

Article

# Mapping Evapotranspiration Coefficients in a Temperate Maritime Climate Using the METRIC Model and Landsat TM

Marios Spiliotopoulos <sup>1,\*</sup>, Nicholas M. Holden <sup>2</sup> and Athanasios Loukas <sup>1</sup>

<sup>1</sup> Laboratory of Hydrology and Aquatic Systems Analysis, Department of Civil Engineering, University of Thessaly, Volos 382 21, Greece; aloukas@uth.gr

<sup>2</sup> UCD School of Biosystems and Food Engineering, University College Dublin, Dublin 4, Ireland; nick.holden@ucd.ie

\* Correspondence: spilioti@uth.gr; Tel.: +30-2-421-074177

Academic Editor: Arjen Y. Hoekstra

Received: 31 August 2016; Accepted: 26 December 2016; Published: 4 January 2017

**Abstract:** The applicability of a land surface temperature (*LST*)-evapotranspiration (*ET*) regression model to estimate *ET* fraction (*ETrF*) was tested in the temperate maritime climate of Central Ireland. In this study, the Mapping *ET* at high Resolution and with Internalized Calibration (METRIC) model was applied to calculate evapotranspiration from a mixed land cover area in Central Ireland. The *ETrF* values estimated on a pixel-by-pixel basis using two different surface roughness maps derived from two different estimates of Leaf Area Index (*LAI*) showed no significant differences. The METRIC based *ETrF* values from a Landsat Enhanced Thematic Mapper Plus (ETM+) image from 12 July 2013 were in similar range with those obtained from a regression model using land surface temperature (*LST*)-*ET* relationship derived from a Landsat 5 Thematic Mapper (TM) image of 17 July 2006. Results indicated that *ETrF* values could be estimated by using *LST* values from Landsat TM, even when stress conditions were prevailing in the region.

**Keywords:** evapotranspiration; crop coefficients; Landsat; METRIC; SEBAL; thermal band; Ireland

---

## 1. Introduction

Regional estimates of Actual Evapotranspiration ( $ET_a$ ) are one of the main components of the hydrological balance and an important factor affecting energy, hydrological, carbon and nutrient cycles.  $ET_a$  can be estimated from physical observations near the ground over homogeneous surfaces using energy balance techniques, such as eddy covariance (EC) and Bowen ratio-energy balance (BREB), or by a soil water balance technique such as surface renewal (SR) [1]. These hydrological and micrometeorological approaches [2–5] prevailed until the mid 1990s [6] where thermal infrared image data from satellites became available for  $ET_a$  mapping by remote sensing using Soil-Vegetation-Atmosphere Transfer (SVAT) models [7].  $ET_a$  models using remote sensing data enable development of real-time management applications for activities such as irrigation management that depend on changes in water status and energy balance at the earth surface through time and by location. Medium- or high-resolution daily evapotranspiration maps are more suitable for regional management than “point” data calculated using balance techniques because they convey the pattern and distribution from local to regional scale.

Satellite data can be used to estimate  $ET_a$  from available energy and sensible heat flux using surface radiation balance and the residual method [8,9]. Mapping EvapoTranspiration at high Resolution and with Internalized Calibration (METRIC) is a variant of the Surface Energy Balance Algorithm for Land (SEBAL) model [10–12] that implements the residual method to calculate  $ET_a$  maps. The METRIC model uses the ET fraction ( $ETrF$ ), which serves the same mathematical purpose as crop coefficient

( $K_c$ ), defined as the ratio of satellite image evapotranspiration to  $ET_r$ , representing the crop type and the development stage of the crop. The concept of reference evapotranspiration ( $ET_r$ ) was introduced to study the evaporative demand of the atmosphere independently of crop type, crop development and management practices.  $ET_r$  values measured or calculated at different locations or in different seasons are comparable as they refer to the evapotranspiration from the same reference surface [13].  $ET_r$  is considered a climatic parameter and can be computed from meteorological data assuming a theoretical  $ET$  calculation from an ideal crop of alfalfa. The FAO Penman–Monteith method is recommended as the best method for determining  $ET_r$  [13].  $K_c$  ( $ET_r,F$  hence) is an adjustment to the  $ET_r$  for non-alfalfa crops taking into account the difference in evapotranspiration between the crop and  $ET_r$ . There may be several  $ET_r,F$  values for a single crop depending on the crop stage of development. Crop coefficients are generally preferable for the estimation of water requirements and water use efficiency and this is the main motivation to use  $ET_r,F$  instead of evapotranspiration [13]. Growth stages, plant physiology and rooting depth are used to define change in crop coefficient through the growing season.

SEBAL and METRIC have been successfully used for many studies around the world [9–11,14]. SEBAL was originally used in Egypt, Spain and Niger [15,16] (predominantly hot, semi-arid to desert climates) and later applied in Mediterranean countries including Turkey [15] and more recently Greece [16,17] and Cyprus [18] (predominantly variants of Mediterranean climate). It has been used in other dry regions of the world; in parts of South America, USA, Europe, Africa, and Asia [19–27]; and, more recently, in cold, high altitude areas [28]. These climates typically have prolonged clear dry weather with a tendency to water stress at times of the year. The objective of this work was to evaluate the application of METRIC to a completely different environment in terms of climate (temperate maritime) and land uses (peatland, permanent grassland, coniferous forest) as found in central Ireland.

## 2. Methods

The study area is County Laois, located in the Midlands Region of Ireland (centred on 53°0' N, 7°24' W; Figure 1). The centre of the county is Slieve Bloom Mountains with a maximum elevation of around 530 m above sea level (ASL) and a plateau to the south-east of the county at 180 to 245 m ASL influence on the climate of the area, particularly temperature and rainfall distribution [29–31]. According to Köppen and Geiger the climate can be characterized as temperate maritime (Cfb). December and January are usually the wettest months, while March, April and June are usually the driest. However, even the driest month still has abundant rainfall compared to Mediterranean and arid climates. At the Durrow weather station (52°50'43" N, 7°23'48" W), there are around eleven raindays per month with 50–60 mm per month in the summer, while the average annual temperature is 9.5 °C with an average maximum of 15.1 °C in July and August and average minimum of 4.4 °C in January. The coldest months are January and February, while July and August are the warmest [30]. The prevailing wind direction is from the southeast to the west. Agriculture is the predominant land-use in the county and that was one of the main reasons for its selection.

The predominant land use is managed grassland, accounting for about 70% of the land area with the remaining land being urban, tillage farming, plantation forestry, uplands including scrub and peatland and low level peatlands [31].

The METRIC model was used to produce  $ET_a$  and  $ET_r,F$  maps for 17 July 2006, utilizing a clear, high quality Landsat 5 TM image with a 30 m spatial resolution (path/row 206/23). Image data were acquiring from the United States Geological Survey (USGS) GloVis tool. These data were chosen because the image was virtually cloud free (rare in Ireland) and represented a time when a water stress had built up due to dry weather in the previous weeks. It should be noted that water stress in the context of a temperate maritime climate is very different from that experienced in semi-arid, Mediterranean and desert climates. Meteorological data from adjacent synoptic weather stations [30] were also used.

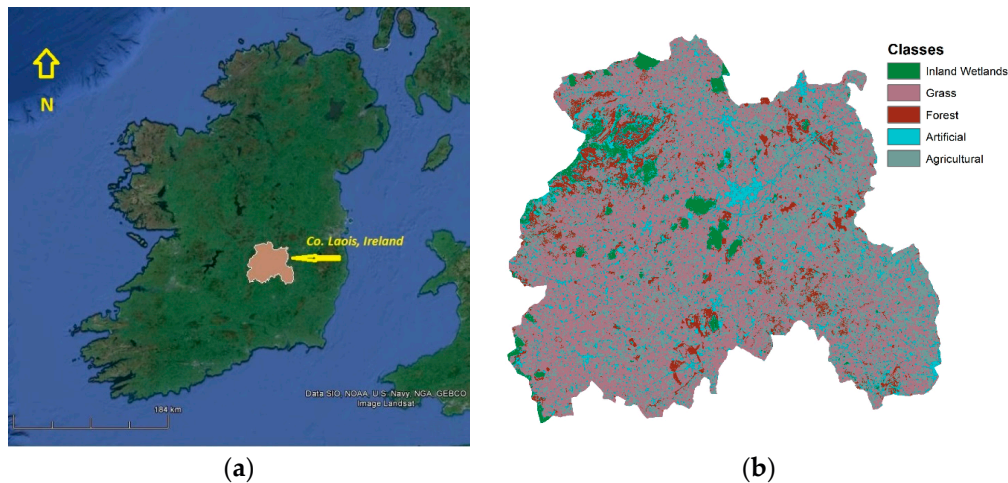


**Figure 1.** Study Area: (a) Laois County, Ireland, Google Earth; and (b) Laois land-use classification map.

Radiometric and geometric correction were applied to the initial TM image deploying the related header file given by USGS [32–35]. Spectral radiance and reflectance image files for each TM band were derived using Digital Numbers (DNs) and Gain and Bias levels for each channel as described at Landsat 7 Science Data Users Handbook [36]. The geometrically corrected images were projected to the Irish map conversion system using the Irish 1965 datum, based on a Transverse Mercator projection and the Airy Modified 1849 Spheroid. The same system is used throughout this study. Each image was finally cropped to the area of interest using the appropriate county shape file. The results of these processes were corrected radiance values for each TM band for the study region. The METRIC model eliminates the need for refined atmospheric correction of surface temperature and albedo due to its internal calibration [37,38], but these steps do improve the overall result [15,39–41].

METRIC is centred on the equation of surface energy balance (Equation (1)):

$$\lambda ET = R_n - G - H \quad (1)$$

where  $\lambda ET$  is the latent heat flux ( $\text{W/m}^2$ ),  $R_n$  is net radiation ( $\text{W/m}^2$ ),  $G$  is soil heat flux ( $\text{W/m}^2$ ) and  $H$  is sensible heat flux ( $\text{W/m}^2$ ). Net radiation was computed from the land surface radiation balance (Equation (2)):

$$R_n = R_{S\downarrow} - \alpha R_{S\downarrow} + R_{L\downarrow} - R_{L\uparrow} - (1 - \varepsilon_o)R_{L\downarrow} \quad (2)$$

where  $\alpha$  is surface albedo,  $R_{S\downarrow}$  ( $\text{W/m}^2$ ) is the incoming solar radiation,  $R_{L\downarrow}$  ( $\text{W/m}^2$ ) is incoming long wave radiation,  $R_{L\uparrow}$  ( $\text{W/m}^2$ ) is the outgoing long wave radiation and  $\varepsilon_o$  is the broad band surface emissivity. Soil heat flux  $G$  ( $\text{W/m}^2$ ) was empirically estimated using the function of Bastiaanssen [15], which is based on albedo, surface temperature and NDVI (Equation (3)):

$$\frac{G}{R_n} = \frac{LST}{\alpha} \left( 0.0038\alpha + 0.0074\alpha^2 \right) \times \left( 1 - 0.98 \times NDVI^4 \right) \quad (3)$$

where  $LST$  is surface temperature ( $^\circ\text{C}$ ) and  $NDVI$  is the widely used Normalized Difference Vegetation Index. The sensible heat flux,  $H$  ( $\text{W/m}^2$ ) for neutral atmospheric conditions was calculated by (Equation (4)):

$$H = \frac{(\rho \times c_p \times dT)}{r_{ah}} \quad (4)$$

where  $\rho$  is air density ( $\text{kg/m}^3$ ) related to atmospheric pressure,  $c_p$  is air specific heat capacity ( $1004 \text{ J}\cdot\text{kg}^{-1}\cdot\text{K}^{-1}$ ),  $dT$  (K) is the temperature difference ( $T_1 - T_2$ ) between two reference heights ( $z_1$  and  $z_2$ ), and  $r_{ah}$  is aerodynamic resistance to heat transport ( $\text{s}\cdot\text{m}^{-1}$ ). Equation (4) has two unknowns,

$r_{ah}$  and  $dT$ , which is normally difficult to solve. The first unknown parameter ( $r_{ah}$ ) was computed for neutral stability as (Equation (5)):

$$r_{ah} = \frac{\left(\ln \frac{z_2}{z_1}\right)}{u^* \times k} \quad (5)$$

where  $z_1$  and  $z_2$  are heights in meters above the zero plane displacement,  $u^*$  is the friction velocity (m/s), and  $k$  is von Karman's constant (0.41). Friction velocity ( $u^*$ ) quantifies the turbulent velocity fluctuations in the air using the logarithmic wind law (Equation (6)) for neutral atmospheric conditions:

$$u^* = \frac{(k \times u_x)}{\left(\ln \frac{z_x}{z_{om}}\right)} \quad (6)$$

where  $k$  is von Karman's constant,  $u_x$  is the wind speed (m/s) at height  $z_x$ , and  $z_{om}$  is the momentum roughness length (m), which is a measure of interaction between the surface and the adjacent layer of air above. Momentum transfer is mainly caused by turbulent drag on roughness elements [42,43].

Wind speed at 200 m above the weather station ( $u_{200}$ ) was calculated then using Equation (6). The height of 200 m is referred in METRIC as the "blending height" [12] (Equation (7)):

$$u_{200} = u^* \times \frac{\left(\ln \frac{200}{z_{om}}\right)}{k} \quad (7)$$

where  $u^*$  is the friction velocity at the weather station. This calculation was done on a spreadsheet [40]. Wind speed ( $u_x$ ) was acquired from the weather station of the study, while momentum roughness length ( $z_{om}$ ) at the station was empirically estimated using the following formula (Equation (8)) [42]:

$$z_{om} = 0.12 \times h \quad (8)$$

where  $h$  is the vegetation height (m).

Friction velocity  $u^*$  for each pixel was finally computed using Equation (9):

$$u^* = \frac{(k \times u_{200})}{\left(\ln \frac{200}{z_{om}}\right)} \quad (9)$$

where  $z_{om}$  is the particular momentum roughness length for each pixel, while  $u_{200}$  is assumed to be constant for all the pixels of the image since it is unaffected by surface features. The momentum roughness length ( $z_{om}$ ) for each pixel was computed using a land-use map and Leaf Area Index ( $LAI$ ) [44]. For agricultural areas,  $z_{om}$  can be calculated as a function of  $LAI$  (Equation (10)):

$$z_{om} = 0.018 \times LAI \quad (10)$$

Non-agricultural areas, have known  $z_{om}$  values [40] and can be assigned using a land-use map (Figure 1b) which has been already created for this study utilizing Corine Land-Cover raster data [45].

METRIC suggests linear change in  $dT$  with  $LST$  [10] meaning that Equation (4) has only two unknown parameters ( $a$  and  $b$ ). This can be expressed as (Equation (11)):

$$dT = a \times LST + b \quad (11)$$

where  $a$  and  $b$  are correlation coefficients, and  $dT$  is defined as the difference between the air temperature very near the surface (at 0.1 m above the zero plane displacement height) and the air temperature at 2.0 m above the zero plane displacement height [40]. To estimate  $a$  and  $b$ , the so-called "cold" and "hot" pixels are selected from the TM image.  $H$  values can be reliably estimated for these pixels which serve as boundary conditions for the total methodology. A "cold" pixel in

METRIC is generally defined as one representing a wet, well-irrigated crop surface with full vegetation cover [10]. A pixel with high value of *LAI* and low *LST* is a very good candidate to be a “cold” pixel. A “hot” pixel is representing a dry, exposed soil, typical of a harvested agricultural field, where all the energy is used to heat the surface ( $ET = 0$ ). A pixel with low values of *LAI* and high *LST* is a very good candidate to be a “hot” pixel. The selection of “hot” pixels is more difficult than the selection of “cold” pixel due to the wide range of temperatures for hot pixel candidates. For the assessment of “cold” and “hot” pixels, a pseudo-colour image was created for each of *LAI*, and *LST* maps in order to acquire a better visualization of the prevailing differences. Finally, cold and hot pixel candidates are recorded and then carefully selected for each case according to the above criteria. *H* was finally computed fitting a line according to Equation (11) and solving Equation (4) assuming neutral atmospheric conditions, meaning that no atmospheric stability or instability was existed. An iterative process was finally used to correct for possible atmospheric instability caused by buoyancy effects of surface heating by applying Monin–Obukhov theory [10,46]. New *dT* values are then computed for the “cold” and “hot” pixels according to the estimated values of *a* and *b*, and a new corrected value for *H* is repeatedly computed while the stability correction is applied until *H* stabilizes. More details about atmospheric stability correction equations can be found in Bastiaanssen [10,11].

Finally, reference *ET* fraction values ( $ET_rF$ ) can be calculated using the standardized ASCE Penman–Monteith equation applied using local meteorological observations assuming  $ET_rF$  is constant over the day (Equation (12)):

$$ET_rF = ET_{ainst}/ET_r \quad (12)$$

where  $ET_{ainst}$  is the instantaneous  $ET_a$  (mm/day) and  $ET_r$  (mm/day) is the evapotranspiration of a known reference crop, usually alfalfa for METRIC. A new image file where each pixel denotes a unique  $ET_rF$  value, with 30 m × 30 m spatial resolution, is the final product of the model. The whole METRIC model is summarized at Figure 2.

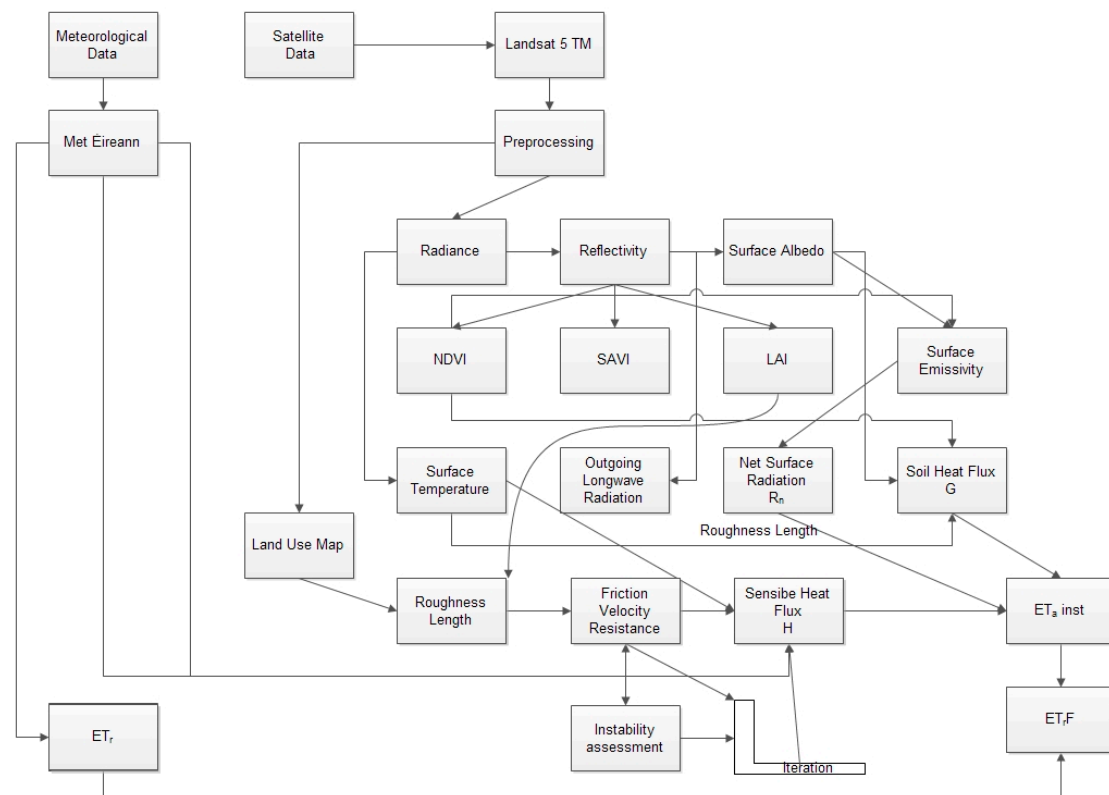


**Figure 2.** METRIC methodology flowchart.

As it can be seen from Figure 2, METRIC model has an obvious complexity, consisting of many sub-models and routines, but, as a residual method, is based on Equation (1) which has a very simple meaning: evapotranspiration can be computed based on  $R_n$ ,  $G$  and  $H$ . Sensible Heat Flux ( $H$ ) is a very important parameter and is generally difficult to compute, but this is where METRIC serves as a solution, utilizing the theory of “boundary” pixels. However, one of the most important steps for the computation of  $H$  is the computation of roughness length, playing a very critical role in the computation of friction velocity resistance (Equations (4)–(6)), and this is where this study mainly contributes [47,48]. The original METRIC model suggests computing roughness length using leaf area index ( $LAI$ ,  $\text{m}^2 \cdot \text{m}^{-2}$ ) multiplied by 0.018, where  $LAI$  is computed as (Equation (13)):

$$LAI = \frac{-\ln\left(\frac{0.69 - SAVI}{0.59}\right)}{0.91} \quad (13)$$

$SAVI$  is computed as (Equation (14)):

$$SAVI = (1 + L) \times \frac{Ch_4 - Ch_3}{(Ch_3 + Ch_4 + L)} \quad (14)$$

where  $Ch_x$  refers to the reflectance expressed as digital number of the Landsat TM channel number ( $x$ ) and  $L$  is an empirical parameter that is difficult to compute for Ireland due to the lack of available images [40]. These relationships (Equations (13) and (14)) were developed for ID, USA, which is very different from the study region so an alternative method for computing  $LAI$  was used derived from Enhanced Vegetation Index 2 ( $EVI2$ ) [49–53], using the formula [50] (Equation (15)):

$$EVI2 = \frac{2.5 \times (Ch_4 - Ch_3)}{Ch_4 + 2.4 \times Ch_3 + 1} \quad (15)$$

and  $LAI$  was finally derived from  $EVI2$  using the method of O’Connell et al. [52,53] (Equation (16)):

$$LAI = \frac{EVI2 - 0.2457}{0.0779} \quad (16)$$

The described methodology has the ability to compute  $LAI$  using  $EVI2$  avoiding the use of  $SAVI$  at the study region which is difficult to compute [40,52,54]. Eventually,  $LAI$  affects the computation of roughness length, which in turn is affecting the computation of friction velocity resistance (Equations (4)–(6)), and finally the computation of  $H$  (Equation (4)). The new methodology of  $LAI$  computation was incorporated into the total METRIC model, and the new results were compared with the METRIC  $ET_rF$ .

Furthermore,  $LST$  values generated using Landsat’s Thematic Mapper (TM) thermal band [40,55] were correlated with  $ET_rF$  values, considering that  $ET_rF$  values are well correlated with thermal units [56–58], while Simplified Surface Energy Balance (SSEB) assumes that actual  $ET$  varies linearly with  $LST$  [59].  $LST$  is a governing parameter in water and energy exchange between land and atmosphere and is also an essential input to most of the irrigation water management activities [60]. Additionally, Sun et al. [61] found linear relationships between  $ET$  and  $LST$  values, while there is a strong indication that maybe there is a significant correlation even if stress conditions are prevailing over regions having maritime climatic conditions [62,63]. A linear equation was finally derived between  $ET_rF$  and  $LST$  values for 17 July 2006 at this study.

For the validation of the derived equation a new image from the same region under the same climatic conditions had to be tested, and that was during the 12 July 2013. The same methodology was followed as that with the initial 2006 image, but with the exception that Landsat 5 was in no operation any more, thus, Landsat ETM+ imagery has been utilized instead. ETM+ has almost the same spectral characteristics as TM [36]. A new METRIC  $ET_rF$  map as well as a new  $LST$  map based on low gain band 6 from ETM+ were then generated for the 12 July 2013 using the described model.

It is crucial to note that a new pair of cold and hot pixel has been used within the model of METRIC. The previous derived linear equation was then applied to the latest case and a new modelled  $ET_rF$  map was generated. METRIC  $ET_rF$  values and modelled  $ET_rF$  values were compared, applying statistics between the two corresponding images.

### 3. Results and Discussion

$ET_rF$  image file product was firstly derived according to METRIC (Figure 3a). The computation of METRIC was implemented again using the new EVI2 based LAI values, and a new  $ET_rF$  map was generated (Figure 3b). Examining Figure 3, is very clear that the two images have almost the same pattern.  $ET_rF$  values using METRIC based LAI are very well correlated with  $ET_rF$  values using O'Connell based LAI, and this assumption can be confirmed by a very high correlation coefficient ( $R = 0.998$ ). It is obvious then that O'Connell based LAI can be incorporated to METRIC model for the next steps of the study.

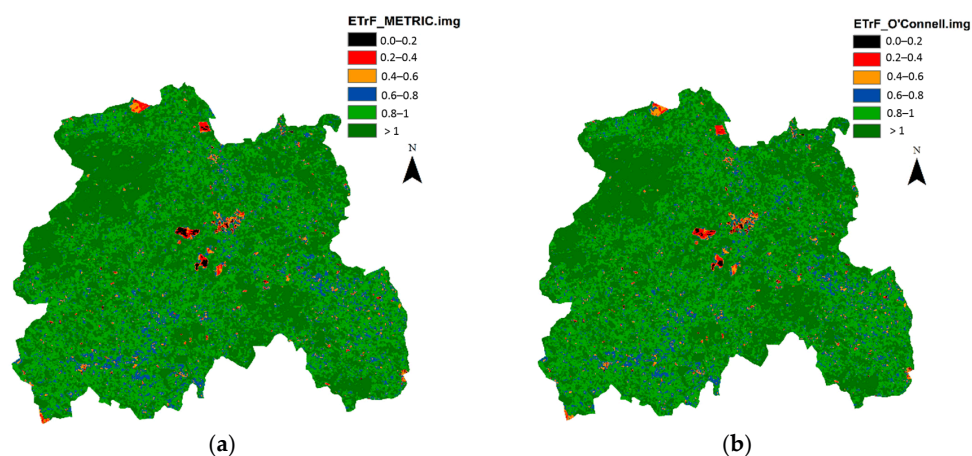


**Figure 3.**  $ET_rF$  maps, 17 July 2006: (a) METRIC based; and (b) O'Connell based.

The relation between  $ET_rF$  and  $LST$  values (Figure 4) using Landsat's 5 TM already generated during METRIC model was then investigated (Figure 5) resulting in the following linear equation (Equation (17)):

$$ET_rF = 19.309 - 0.0614 \times LST \quad (17)$$

Equation (17) explained the relation between  $ET_rF$  and  $LST$  values very satisfactorily ( $R^2 = 0.89$ ).

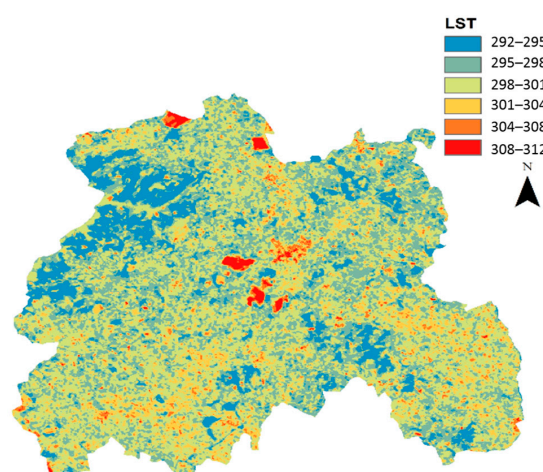


**Figure 4.**  $LST$  map (K) (17 July 2006).

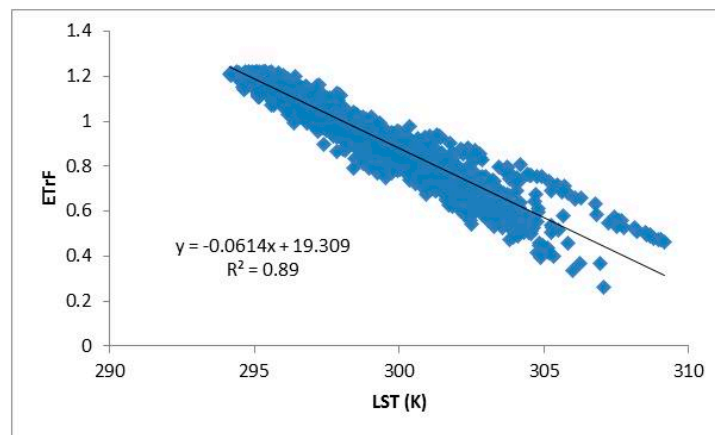


**Figure 5.** Relation between  $LST$  and  $ET_rF$  values (17 July 2006).

Equation (17) was then tested by applying to the initial  $LST$  image file, producing a new modelled  $ET_rF$  image as shown in Figure 6. The values of the new map have an average value of 0.64 ( $std = 0.18$ ) while the initial METRIC map has an average of 0.72 ( $std = 0.16$ ). The total correlation between the initial and final image map applied to a number of 1,909,074 pixels is high ( $R = 0.63$ ). Image differencing defined as the subtraction of the pixel digital values of the first image recorded at one date from the corresponding pixel values of the second image was applied then [64–67]. The results showed that the difference image file between METRIC  $ET_rF$  map and the modelled one has an average of 0.02 ( $std = 0.06$ ).

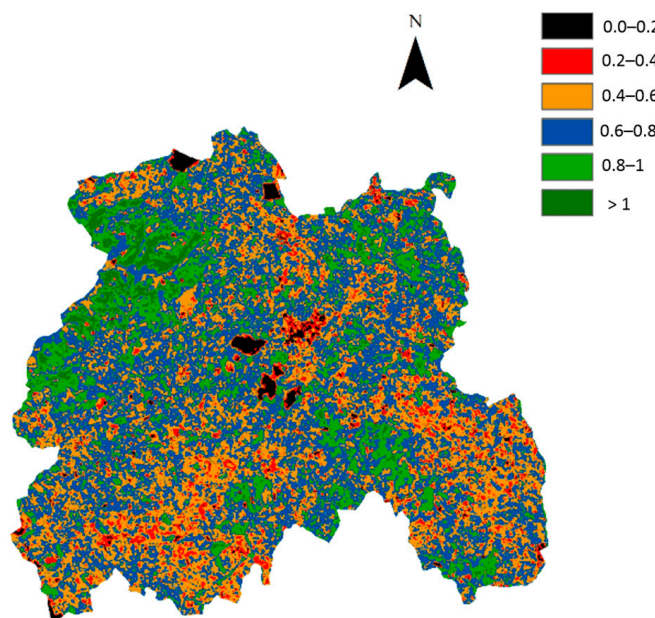


**Figure 6.** Modelled  $ET_rF$  values (17 July 2006).

A validation of Equation (17) was finally implemented using the new case of 12 July 2013. Two  $ET_rF$  maps were generated applying METRIC (average value 0.61) and the model (Equation (17)) respectively (average value 0.60), and the results are shown in Figure 7. The total correlation between METRIC and model based  $ET_rF$  values is high ( $R = 0.88$ ).

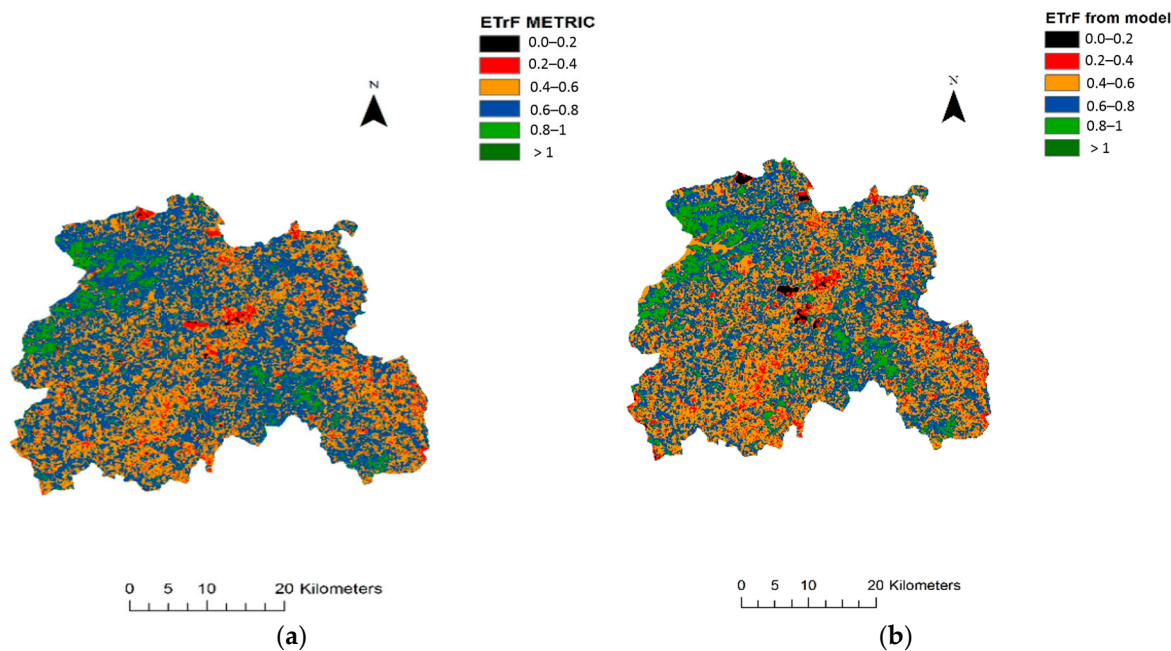


**Figure 7.** ET<sub>r</sub>F maps of 12 July 2013 at Laois Co: (a) METRIC based; and (b) O'Connell based.

The mean value for the difference image obtaining after subtracting the two previous images (Figure 8a) is 0.005 ( $std = 0.07$ ). It is clear that larger differences (in red colour) can be seen over regions defined as inland water at Figure 1. For that reason, separate regression models were developed for three land cover types. More specifically, grass, forest and agricultural were merged into one class (GFA), while artificial (AR) and inland wetlands (IW) used as they were. The result of these regressions is summarized by the following equations ( $R^2$  values  $> 0.90$ ):

$$ET_rF = 19.161 - 0.0610 \times LST \text{ (GFA)} \quad (18)$$

$$ET_rF = 19.944 - 0.0637 \times LST \text{ (AR)} \quad (19)$$

$$ET_rF = 20.288 - 0.0642 \times LST \text{ (IW)} \quad (20)$$

Comparisons among model outputs using Equations (17)–(20) were then conducted on a pixel-by-pixel basis for the three classes. The analysis showed that the resulted ET<sub>r</sub>F values were not significant different between GFA and AR classes, but a remarkable variation appeared when using Equation (20). It was therefore decided to utilize Equation (17) throughout the LST image except the pixels belonging to IW class. A mask was created for those pixels, and a separate equation (Equation (20)) was used instead. The whole ET<sub>r</sub>F image map was a result of merging the two previous images resulting from Equations (17) and (20) into one. After applying the previous methodology to the new modelled ET<sub>r</sub>F image file, a new difference image file between METRIC and modelled ET<sub>r</sub>F was generated (Figure 8b). The results finally showed a clear improvement (difference mean value = 0.004,  $std = 0.06$ ) as might have been expected.

Interestingly, the evaluation of the energy balance components, such as the net radiation and the sensible and latent heat fluxes, is characterized by significant uncertainties related to surfaces heterogeneity [68]. Therefore, a new pixel oriented parameterization would be required for IW surfaces [69]. This issue must be further considered as new sensors in higher spatial and temporal resolutions become available, contributing to the development of new land use classifications identical for energy balance applications.

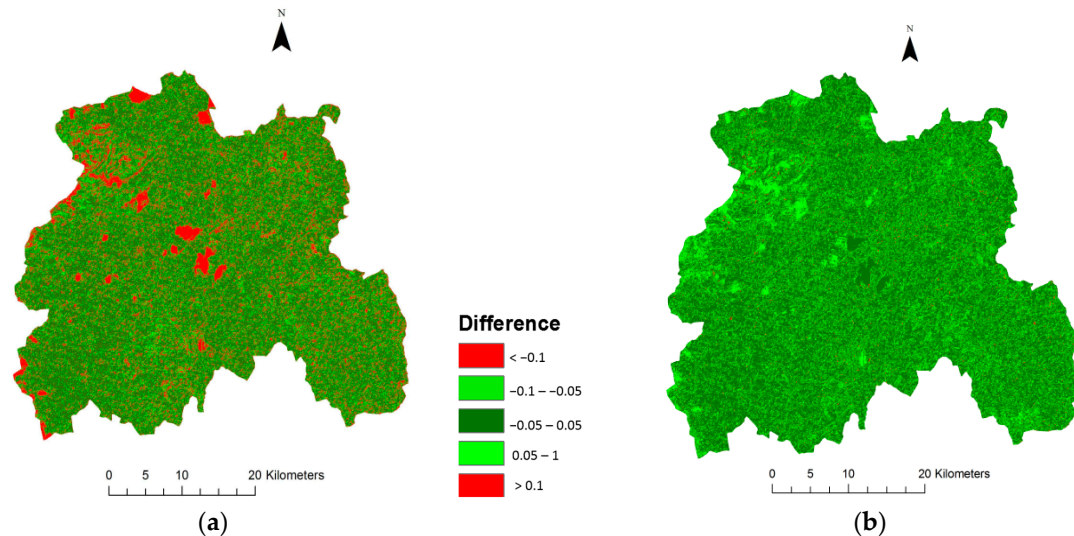


**Figure 8.** Difference between METRIC and modelled  $ET_rF$  (12 July 2013): (a) initial case; and (b) after masking IW class.

Summarizing, METRIC model showed reasonable results estimating the  $ET_rF$  values on a pixel by pixel basis, but the main weakness of this study remains the absence of real measured evapotranspiration data for the appropriate validation. However, METRIC is very well established between other energy balance models for many years now [9]. It also noteworthy that Earth Engine Evapotranspiration Flux (EEFlux) which is a web-based tool operating on the Google Earth Engine and computational cloud uses METRIC model as foundation [70].

Another limitation of the study is that the model has only been applied to a small scale. However, after establishing the appropriate regression equations of the model, the same equations might be applied to other sensors [71]. A well-known procedure for taking advantage of a better temporal resolution is called downscaling [72,73]. It has been suggested [73–75] that is feasible to apply various downscaling methods to combine MODIS and Landsat imagery in order to obtain both high temporal and high spatial  $ET$  resolutions. Using a daily temporal resolution like MODIS [75,76] it is easy to exploit new images and apply the model to a new data set, strengthening the applicability of the procedure. Furthermore, introducing hyperspectral data is possible to improve the accuracy of  $LST$  computation, while the use of microwave data during the days affected by weather could make an  $LST$  estimation feasible. An integrated use of multi-source, multi-scale remote sensing data to expand temporal scale of  $ET_rF$  based on the characteristics of study area, is a breakthrough for future research [77–79]. On such basis, this study provides the framework for future analysis elsewhere.

#### 4. Conclusions

In this study, METRIC model was applied to compute  $ET_rF$  values in a temperate maritime climate. In order to examine the proposed model, Laois Co. central Ireland has been selected mainly because it is a typical regional agricultural region. Landsat TM, ETM+ and meteorological data have been used together in order to compute energy balance parameters necessary for the final computation of  $ET_rF$  values. The results show reasonable spatial variations in correspondence with the already known land-use classes of the region. Then, METRIC model was implemented using locally adapted LAI values, given as a function of EVI2. LAI is much easier to compute using the proposed formula, since it is not dependent on time-series of remotely sensed physical parameters which is difficult to obtain. There was a significant positive correlation.

Furthermore, an approach based on the correlation between  $LST$  and  $ET_rF$  values has been introduced, which shows high performance in estimating  $ET_rF$  values after applying the related regression model ( $R^2 = 0.89$ ). The approach was based on a Landsat TM image taken on 17 July 2006.

A linear equation explained that relation was validated using a new Landsat ETM+ image taken on 12 July 2013. Subtracting the new modelled  $ET_rF$  image from METRIC  $ET_rF$  image, the findings were reasonable. However the performance was not ideal especially on inland water pixels, leading to a different approach, where those pixels were masked and excluded from the initial regression. Another regression has been performed only for those pixels belonging to IW class, and then the two results were merged. The final difference image map showed a clear improvement in comparison with the first approach.

The most important limitation of the study is the fact that there is no available in-situ validation data. Another limitation is that the model remains local in nature as it uses a locally derived LAI equation and a regression model derived from one image. However, when using downscaling techniques and different sensors in higher spatial and temporal resolutions, it is feasible to take advantage of the derived regression equations. Future work will concentrate on those downscaling techniques, combining with the use of new thermal in-situ sensors. Further studies, which take land-use classification into account, will also need to be undertaken, because this study showed a remarkable sensitivity in that aspect.

In conclusion, a regression between METRIC  $ET_rF$  and  $LST$  values is suggested using Landsat imagery, applied in a temperate maritime climate. Although METRIC is a promising tool for mapping  $ET_rF$  values accurately worldwide, additional evaluation is needed under a variety of crop, land-use and weather conditions to fully assess its capability to accurately estimate spatially distributed  $ET_rF$  values.

**Acknowledgments:** This work was supported by ESSEM COST ES1106: Assessment of EUROpean AGRICulture WATer use and trade under climate change (EURO-AGRIWAT). The authors acknowledge Met Éireann for providing meteorological data as well as NASA next generation metadata and service discovery tool “Reverb” for providing satellite data. An initial version of this paper has been presented at the EURO-AGRIWAT Conference: “Water Footprint of agricultural products: Progress, challenges and solutions”, 7–9 March 2016, Wageningen, The Netherlands.

**Author Contributions:** Marios Spiliopoulos and Nicholas M. Holden conceived and designed the study; Athanasios Loukas provided the method and guided the entire study; Nicholas M. Holden contributed reagents/materials/analysis tools; Marios Spiliopoulos processed, analysed the satellite data and wrote the first draft; Athanasios Loukas and Nicholas M. Holden were responsible for the revised version of the manuscript.

**Conflicts of Interest:** The authors declare no conflict of interest.

## References

1. Wonsook, H.; Prasanna, H.G.; Terry, A.H. A review of downscaling methods for remote sensing-based irrigation management: Part I. *Irrig. Sci.* **2000**. [[CrossRef](#)]
2. Penman, H.L. *Vegetation and Hydrology*; Tech. Comm. No. 53; Commonwealth Bureau of Soils: Harpenden, UK, 1963.
3. Priestley, C.H.B.; Taylor, R.J. On the assessment of surface heat flux and evaporation using large-scale parameters. *Mon. Weather Rev.* **1972**, *100*, 81–92. [[CrossRef](#)]
4. Liakatas, A.; Anadranistikis, M. *Derived Meteorological Parameters: Evapotranspiration, Hydroscope: Creation of a National Databank for Hydrological and Meteorological Information*; Contractor: Dep. of Water Resources, Hydraulic and Maritime Engineering—N.T.U.A, Report 5/4; Hellenic National Meteorological Service: Athens, Greece, 1992; p. 31.
5. Shuttleworth, W.J. Evaporation. In *Handbook of Hydrology*; Maidment, D.R., Ed.; McGraw Hill: New York, NY, USA, 1993; pp. 4.1–4.53.
6. Tsakiris, G. Water Resources: 1. In *Technical Hydrology*; Simmetria Publications: Athens, Greece, 1995. (In Greek)
7. Olioso, A.; Chauki, H.; Courault, D.; Wigneron, J.P. Estimation of evapotranspiration and photosynthesis by assimilation of remote sensing data into SVAT models. *Remote Sens. Environ.* **1999**, *68*, 341–356. [[CrossRef](#)]
8. Morse, A.; Kramber, W.J.; Allen, R.G.; Tasumi, M. Use of the METRIC evapotranspiration model to compute water use by irrigated agriculture in Idaho. In Proceedings of the 2004 International Geophysical and Remote Sensing Symposium, Anchorage, AK, USA, 20–24 September 2004.

9. Li, Z.L.; Tang, R.; Wan, Z.; Bi, Y.; Zhou, C.; Tang, B.; Yan, G.; Zhang, X. A review of current methodologies for regional evapotranspiration estimation from remotely sensed data. *Sensors* **2009**, *9*, 3801–3853. [[CrossRef](#)] [[PubMed](#)]
10. Bastiaanssen, W.G.M.; Menenti, M.; Feddes, R.A.; Holtslag, A.A.M. A remote sensing surface energy balance algorithm for land (SEBAL): 1. Formulation. *J. Hydrol.* **1998**, *212*–*213*, 198–212. [[CrossRef](#)]
11. Bastiaanssen, W.G.M.; Pelgrum, H.; Wang, J.; Ma, Y.; Moreno, J.; Roerink, G.J.; van der Wal, T. The surface energy balance algorithm for land (SEBAL): Part 2 validation. *J. Hydrol.* **1998**, *212*–*213*, 213–229. [[CrossRef](#)]
12. Allen, R.G.; Tasumi, M.; Trezza, R. Satellite-based energy balance for mapping evapotranspiration with internalized calibration (METRIC)—Model. *ASCE J. Irrig. Drain. Eng.* **2007**, *133*, 380–394. [[CrossRef](#)]
13. Pereira, L.S.; Allen, R.G.; Smith, M.; Raes, D. Crop evapotranspiration estimation with FAO56: Past and future. *Agric. Water Manag.* **2015**, *147*, 4–20. [[CrossRef](#)]
14. Trezza, R.; Allen, R.G.; Tasumi, M. Estimation of actual evapotranspiration along the Middle Rio Grande of New Mexico using MODIS and Landsat imagery with the METRIC model. *Remote Sens.* **2013**, *5*, 5397–5423. [[CrossRef](#)]
15. Bastiaanssen, W.G.M. SEBAL-based sensible and latent heat fluxes in the irrigated Gediz Basin, Turkey. *J. Hydrol.* **2000**, *229*, 87–100. [[CrossRef](#)]
16. Alexandridis, T.K.; Chemin, Y.; Cherif, I.; Tsakoumis, G.; Galanis, G.; Arampatzis, G.; Zalidis, G.C.; Silleos, N.G.; Stavrinos, E. Improving spatial resolution of agricultural water use estimation using ALOS AVNIR-2 imagery. In Proceedings of the ALOS Principal Investigators Symposium, Rhodes, Greece, 3–7 November 2008; p. 8.
17. Spiliotopoulos, M.; Loukas, A.; Michalopoulou, H. Contribution to the study of regional actual evapotranspiration with the use of surface energy balance and remote sensing for central Greece. In *Advances in Meteorology, Climatology and Atmospheric Physics*; Springer: Berlin/Heidelberg, Germany, 2013; pp. 309–315.
18. Papadavid, G.; Perdikou, S.; Hadjimitsis, M.; Hadjimitsis, D. Remote sensing applications for planning irrigation management. The use of SEBAL methodology for estimating crop evapotranspiration in Cyprus. *Environ. Clim. Technol.* **2012**, *9*, 17–21.
19. Liou, Y.A.; Kar, S.K. Evapotranspiration estimation with remote sensing and various surface energy balance algorithms—A review. *Energies* **2014**, *7*, 2821–2849. [[CrossRef](#)]
20. Morton, C.G.; Huntington, J.L.; Pohll, G.M.; Allen, R.G.; Mcgwire, K.C.; Bassett, S.D. Assessing calibration uncertainty and automation for estimating evapotranspiration from agricultural areas using METRIC. *J. Am. Water Resour. Assoc.* **2013**, *49*, 549–562. [[CrossRef](#)]
21. Teixeira, A.H.; Bastiaanssen, W.G.M.; Ahmad, M.D.; Bos, M.G. Reviewing SEBAL input parameters for assessing evapotranspiration and water productivity for the Low-Middle Sao Francisco River basin, Brazil Part A: Calibration and validation. *Agric. For. Meteorol.* **2009**, *149*, 462–476. [[CrossRef](#)]
22. Carrillo-Rojas, G.; Silva, B.; Córdova, M.; Cáceres, R.; Bendix, J. Dynamic mapping of evapotranspiration using an energy balance-based model over an andean páramo catchment of southern Ecuador. *Remote Sens.* **2016**, *8*, 160. [[CrossRef](#)]
23. Al Zayed, I.S.; Elagib, N.A.; Ribbe, L.; Heinrich, J. Satellite-based evapotranspiration over Gezira Irrigation Scheme, Sudan: A comparative study. *Agric. Water Manag.* **2016**, *177*, 66–76. [[CrossRef](#)]
24. Lian, J.; Huang, M. Comparison of three remote sensing based models to estimate evapotranspiration in an oasis-desert region. *Agric. Water Manag.* **2016**, *165*, 153–162. [[CrossRef](#)]
25. Liaqat, U.W.; Choi, M. Surface energy fluxes in the Northeast Asia ecosystem: SEBS and METRIC models using Landsat satellite images. *Agric. For. Meteorol.* **2015**, *214*–*215*, 60–79. [[CrossRef](#)]
26. Bala, A.; Rawat, K.S.; Misra, A.K.; Srivastava, A. Assessment and validation of evapotranspiration using SEBAL algorithm and Lysimeter data of IARI agricultural farm, India. *Geocarto Int.* **2016**, *31*, 739–764. [[CrossRef](#)]
27. Jaber, H.S.; Mansor, S.; Pradhan, B.; Ahmad, N. Evaluation of SEBAL model for Evapotranspiration mapping in Iraq using remote sensing and GIS. *Int. J. Appl. Eng. Res.* **2016**, *11*, 3950–3955.
28. Chang, Y.; Ding, Y.; Zhao, Q.; Zhang, S. Remote estimation of terrestrial evapotranspiration by Landsat 5 TM and the SEBAL model in cold and high-altitude regions: A case study of the upper reach of the Shule River Basin, China. *Hydrol. Process.* **2016**. [[CrossRef](#)]
29. CSO. Available online: <http://www.cso.ie> (accessed on 5 July 2016).
30. Met Éireann. Available online: <http://www.met.ie> (accessed on 5 July 2016).

31. Laois County Council (Laois County Development Plan, Appendix 6 Landscape Character Assessment, 2011–2017). Available online: <http://www.laois.ie/media/Media,7818,en.pdf> (accessed on 5 July 2016).
32. Price, J.C. Calibration of satellite radiometers and the comparison of vegetation indices. *Remote Sens. Environ.* **1987**, *21*, 15–27. [[CrossRef](#)]
33. Jensen, J.R. *Introductory Digital Image Processing: A Remote Sensing Perspective*, 2nd ed.; Prentice Hall: Upper Saddle River, NJ, USA, 1996; p. 316.
34. Chander, G.; Markham, B. Revised Landsat-5 TM radiometric calibration procedures and post-calibration dynamic ranges. *IEEE Trans. Geosci. Remote Sens.* **2003**, *41*, 2674–2677. [[CrossRef](#)]
35. Riaño, D.; Chuvieco, E.; Salas, J.; Aguado, I. Assessment of different topographic corrections in Landsat-TM data for mapping vegetation types. *IEEE Trans. Geosci. Remote Sens.* **2003**, *41*, 1056–1061. [[CrossRef](#)]
36. Landsat 7 Science Data Users Handbook. Project Science Office at NASA’s Goddard Space Flight Center in Greenbelt, MD, USA. Available online: [http://landsat.gsfc.nasa.gov/wp-content/uploads/2016/08/Landsat7\\_Handbook.pdf](http://landsat.gsfc.nasa.gov/wp-content/uploads/2016/08/Landsat7_Handbook.pdf) (accessed on 29 December 2016).
37. Bastiaanssen, W.G.M.; Noordman, E.J.M.; Pelgrum, H.; Davids, G.; Thoreson, B.P.; Allen, R.G. SEBAL Model with Remotely Sensed Data to Improve Water Resources Management under Actual Field Conditions. *ASCE J. Irrig. Drain. Eng.* **2005**, *131*, 85–93. [[CrossRef](#)]
38. Allen, R.G.; Tasumi, M.; Morse, A.; Trezza, R.; Wright, J.L.; Bastiaanssen, W.; Kramber, W.; Lorite, I.; Robinson, C.W. Satellite-based energy balance for mapping evapotranspiration with internalized calibration (METRIC)—Applications. *J. Irrig. Drain. Eng.* **2007**, *133*, 395–406. [[CrossRef](#)]
39. Kaufman, Y.J. The atmospheric effect on remote sensing and its correction. In *Theory and Applications of Optical Remote Sensing*; Asrar, G., Ed.; John Wiley and Sons: Hoboken, NJ, USA, 1989.
40. Allen, R.; Tasumi, M.; Trezza, R.; Waters, R.; Bastiaanssen, W. *Surface Energy Balance Algorithm for Land (SEBAL)–Advanced Training and Users Manual*; Idaho Department of Water Resources, University of Idaho: Moscow, ID, USA, 2002.
41. Kübert, C.; Conrad, C.; Falk, U.; Hendrickx, J. Assessing the impact of atmospheric corrections on modeling surface energy balance fluxes with SEBAL. In *Global Change and Water Resources in West Africa the German-African GLOWA Projects, Proceedings of the International Conference, Ouagadougou, Burkina Faso, 25–28 August 2008*; Federal Ministry of Education and Research (BMBF): Bonn, Germany, 2008.
42. Brutsaert, W. *Evaporation into the Atmosphere, Theory, History, and Applications*; D. Reidel: Boston, MA, USA, 1982; p. 299.
43. Yang, R.; Friedl, M.A. Determination of roughness lengths for heat and momentum over boreal forests. *Bound. Layer Meteorol.* **2003**, *107*, 581–603. [[CrossRef](#)]
44. Paul, G.; Gowda, P.H.; Vara Prasad, P.V.; Howell, T.A.; Aiken, R.M.; Neale, C.M.U. Investigating the influence of roughness length for heat transport ( $z_{oh}$ ) on the performance of SEBAL in semi-arid irrigated and dry land agricultural systems. *J. Hydrol.* **2014**, *509*, 231–234. [[CrossRef](#)]
45. Environmental Protection Agency (EPA). *CORINE Land Cover 2000 Update (Ireland) Final Report 2013*; EPA: Johnstown Castle, Ireland, 2013.
46. Monin, A.S.; Obukhov, A.M. Basic laws of turbulent mixing in the surface layer of the atmosphere. *Tr. Akad. Nauk SSSR Geofiz. Inst.* **1954**, *24*, 163–187.
47. Pôças, I.; Paço, T.A.; Cunha, M.; Andrade, J.A.; Silvestre, J.; Sousa, A.; Santos, F.L.; Pereira, L.S.; Allen, R.G. Satellite-based evapotranspiration of a super-intensive olive orchard: Application of METRIC algorithms. *Biosyst. Eng.* **2014**, *128*, 69–81. [[CrossRef](#)]
48. Paço, T.A.; Pôças, I.; Cunha, M.; Silvestre, J.C.; Santos, F.L.; Paredes, P.; Pereira, L.S. Evapotranspiration and crop coefficients for a super intensive olive orchard. An application of SIMDualKc and METRIC models using ground and satellite observations. *J. Hydrol.* **2014**, *519*, 2067–2080. [[CrossRef](#)]
49. Huete, A.; Didan, K.; Miura, T.; Rodriguez, E.P.; Gao, X.; Ferreira, L.G. Overview of the radiometric and biophysical performance of the MODIS vegetation indices. *Remote Sens. Environ.* **2002**, *83*, 195–213. [[CrossRef](#)]
50. Jiang, Z.; Huete, A.; Didan, K.; Miura, T. Development of a two-band enhanced vegetation index without a blue band. *Remote Sens. Environ.* **2008**, *112*, 3833–3845. [[CrossRef](#)]
51. Rocha, A.; Shaver, G. Advantages of a two band EVI calculated from solar and photosynthetically active radiation fluxes. *Agric. For. Meteorol.* **2009**, *149*, 1560–1563. [[CrossRef](#)]

52. O’Connell, J.; Connolly, J.; Holden, N.M. A monitoring protocol for vegetation change on Irish peatland and heath. *Int. J. Appl. Earth Obs. Geoinf.* **2014**, *31*, 130–142. [[CrossRef](#)]
53. O’Connell, J.; Connolly, J.; Vermote, E.F.; Holden, N.M. Radiometric normalization for change detection in peatlands: a modified temporal invariant cluster approach. *Int. J. Remote Sens.* **2013**, *34*, 2905–2924. [[CrossRef](#)]
54. Palle, E.; Butler, C. Sunshine records from Ireland: cloud factors and possible links to solar activity and cosmic rays. *Int. J. Climatol.* **2001**, *21*, 709–729. [[CrossRef](#)]
55. Wukelic, G.E.; Gibbons, D.E.; Martucci, L.M.; Foote, H.P. Radiometric calibration of Landsat Thematic Mapper thermal band. *Remote Sens. Environ.* **1989**, *28*, 339–347. [[CrossRef](#)]
56. Martínez-Cob, A. Use of thermal units to estimate corn crop coefficients under semiarid climatic conditions. *Irrig. Sci.* **2008**, *26*, 335–345.
57. Bautista-Capetillo, C.; Zavala, M.; Martínez-Cob, A. Using thermal units for crop coefficient estimation and irrigation scheduling improves yield and water productivity of corn (*Zea mays* L.). *J. Irrig. Drain. Eng.* **2013**, *139*, 214–220. [[CrossRef](#)]
58. Dhungel, R.; Allen, R.G.; Trezza, R.; Robison, C.W. Comparison of latent heat flux using aerodynamic methods and using the penman–monteith method with satellite-based surface energy balance. *Remote Sens.* **2014**, *6*, 8844–8877. [[CrossRef](#)]
59. Cai, X.; Sharma, B.R.; Matin, M.A.; Sharma, D.; Gunasinghe, S. *An Assessment of Crop Water Productivity in the Indus and Ganges River Basins: Current Status and Scope for Improvement*; International Water Management Institute (IWMI): Colombo, Sri Lanka, 2010; p. 22.
60. Nikam, B.R.; Ibragimov, F.; Chouksey, A.; Aggarwal, S.P. Retrieval of land surface temperature from Landsat 8 TIRS for the command area of Mula irrigation project. *Environ. Earth Sci.* **2016**, *16*, 1169. [[CrossRef](#)]
61. Hopkins, Z.; Wang, Q.; Batkhishig, O.; Ouyang, Z. Relationship between evapotranspiration and land surface temperature under energy- and water-limited conditions in dry and cold climates. *Adv. Meteorol.* **2016**. [[CrossRef](#)]
62. Hopkins, A.; Del Prado, A. Implications of climate change for grasslands in Europe, impacts, adaptations and mitigation options: a review. *Grass Forage Sci.* **2007**, *62*, 118–126. [[CrossRef](#)]
63. Gilliland, T.J.; Farrell, A.D.; Grogan, D. Differential responses to climatic conditions in Ireland by five grass species. In *Grassland Farming and Land Management Systems in Mountainous Regions, Proceedings of the 16th Symposium of the European Grassland Federation, Gumpenstein, Austria, 29–31 August 2011*; Potch, E.M., Krautzer, B., Hopkins, A., Eds.; Agricultural Research and Education Center (AREC) Raumberg-Gumpenstein: Irdning, Austria, 2011; Volume 16, pp. 217–219.
64. Congalton, R.G.; Green, K. *Assessing the Accuracy of Remotely Sensed Data: Principles and Practices*; Lewis Publishers: Boca Raton, FL, USA, 1999; p. 137.
65. Foody, G.M. What is the difference between two maps? A remote sensor’s view. *J. Geogr. Syst.* **2006**, *8*, 119–130. [[CrossRef](#)]
66. Myint, S.W.; Yuan, M.; Cerveny, R.S.; Giri, C.P. Comparison of remote sensing image processing techniques to identify tornado damage areas from Landsat TM data. *Sensors* **2008**, *8*, 1128–1156. [[CrossRef](#)] [[PubMed](#)]
67. Hayes, D.J.; Sader, S.A. Comparison of change-detection techniques for monitoring tropical forest clearing and vegetation regrowth in a time series. *Photogramm. Eng. Remote Sens.* **2001**, *67*, 1067–1075.
68. Scavone, G.; Sánchez, J.M.; Telesca, V.; Caselles, V.; Copertino, V.A.; Pastore, V.; Valor, E. Pixel-oriented land use classification in energy balance modelling. *Hydrol. Process.* **2014**, *28*, 25–36. [[CrossRef](#)]
69. Quinn, N.W.T.; Epshtain, O. Seasonally-managed wetland footprint delineation using landsat ETM+ satellite imagery. *Environ. Model. Softw.* **2014**, *54*, 9–23. [[CrossRef](#)]
70. Allen, R.; Morton, C.; Kamble, B.; Kilic, A.; Huntington, J.; Thau, D.; Gorelick, N.; Erickson, T.; Moore, R.; Trezza, R.; et al. EEFlux: A Landsat-based Evapotranspiration mapping tool on the Google Earth Engine. In Proceedings of the Joint ASABE/IA Irrigation Symposium 2015: Emerging Technologies for Sustainable Irrigation, Long Beach, CA, USA, 10–12 November 2015; pp. 424–433.
71. Spiliotopoulos, M.; Loukas, A.; Mylopoulos, N. A new remote sensing procedure for the estimation of crop water requirements. In Proceedings of the Third International Conference on Remote Sensing and Geoinformation of the Environment, Paphos, Cyprus, 16–19 March 2015.
72. Bierkens, M.F.P.; Finke, P.A.; Willigen, D.E. *Upscaling and Downscaling Methods for Environmental Research*; Wageningen University and Research Centre: Dordrecht, The Netherlands, 2000.

73. Hong, H.; Hendrickx, J.; Borchers, B. Down-scaling of SEBAL derived evapotranspiration maps from MODIS (250) to Landsat (30 m) scales. *Int. J. Remote Sens.* **2012**, *32*, 6457–6477. [[CrossRef](#)]
74. Spiliotopoulos, M.; Adaktylou, N.; Loukas, A.; Michalopoulou, H.; Mylopoulos, N.; Toulios, L. A spatial downscaling procedure of MODIS derived actual evapotranspiration using Landsat images at central Greece. In *First International Conference on Remote Sensing and Geoinformation of the Environment (RSCy2013)*; SPIE Conference Proceedings; The International Society for Optical Engineering (SPIE): Bellingham, WA, USA, 2013; Volume 8795.
75. Bhattacharai, N.; Quackenbush, L.J.; Dougherty, M.; Marzen, L.J. A simple Landsat–MODIS fusion approach for monitoring seasonal evapotranspiration at 30 m spatial resolution. *Int. J. Remote Sens.* **2015**, *36*, 115–143. [[CrossRef](#)]
76. Ke, Y.; Im, J.; Park, S.; Gong, H. Downscaling of MODIS One kilometer evapotranspiration using Landsat-8 data and machine learning approaches. *Remote Sens.* **2016**, *8*, 215. [[CrossRef](#)]
77. Hendrickx, J.M.H.; Allen, R.G.; Brower, A.; Byrd, A.R.; Hong, S.H.; Ogden, F.L.; Pradhan, N.R.; Robison, C.W.; Toll, D.; Trezza, R.; et al. Benchmarking optical/thermal satellite imagery for estimating evapotranspiration and soil moisture in decision support tools. *J. Am. Water Resour. Assoc.* **2016**, *52*, 89–119. [[CrossRef](#)]
78. Xia, H.; Li, A.; Zhao, W.; Bian, J. Review of temporal scale expansion for evapotranspiration retrieved by remote sensing data. *Trans. Chin. Soc. Agric. Eng.* **2015**, *31*, 162–173.
79. Navarro, A.; Rolim, J.; Miguel, I.; Catalão, J.; Silva, J.; Painho, M.; Vekerdy, Z. Crop monitoring based on SPOT-5 Take-5 and sentinel-1A data for the estimation of crop water requirements. *Remote Sens.* **2016**, *8*, 525. [[CrossRef](#)]



© 2017 by the authors; licensee MDPI, Basel, Switzerland. This article is an open access article distributed under the terms and conditions of the Creative Commons Attribution (CC-BY) license (<http://creativecommons.org/licenses/by/4.0/>).